PCCP

PAPER

View Article Online
View Journal

Check for updates

Cite this: DOI: 10.1039/c9cp00402e

Theoretical study on the light-emitting mechanism of circularly polarized luminescence molecules with both thermally activated delayed fluorescence and aggregation-induced emission†

Xiu Yin,[a] Jian-Zhong Fan,[b] Jie Liu,[b] Lei Cai,[b] Hao Sun,[a] Yu-Ping Sun,*[a] Chuan-Kui Wang*[b] and Li-Li Lin*[b]

Received 22nd January 2019,
Accepted 4th March 2019

DOI: 10.1039/c9cp00402e

rsc.li/pccp

Circularly polarized luminescence molecules with both thermally activated delayed fluorescence (TADF) and aggregation-induced emission (AIE) have been reported recently and are thought as potential candidates for circular polarized organic light-emitting diodes. Since the study of these kinds of systems is quite limited, it is of great importance to reveal the relationship between the geometry and the light-emitting mechanism. In this paper, the TADF and AIE mechanisms were studied based on the study of a series of binaphthalene-containing luminogenic enantiomers in both toluene and solid phases. It was found that there was no influence on the light-emitting properties of enantiomers except for the electronic circular dichroism (ECD). The radiative rates for both molecules were enhanced in the solid phase, while the non-radiative rates were significantly suppressed. Both factors can induce the AIE phenomenon. Based on the calculation of the decay rates and adiabatic excitation energy of the excited states, we found that the TADF mechanisms of the two molecules were different. One is realized by the up-conversion process between S_1 and T_1, while a two-step process is involved for the other. Our theoretical research successfully elucidates the experimental measurement and illustrates the AIE and TADF mechanism, which could provide valuable insights for the design of highly efficient CPL emitters.

Published on 08 March 2019. Downloaded by Institute of Chemistry, CAS on 3/26/2019 2:21:59 AM.

Introduction

Circularly polarized luminescence (CPL) materials with potential application in optical data storage,[1] optical recognition sensors,[2,3] quantum computing,[4] optical communication for spintronics[5] and 3D displays[6] have attracted great attention for their potential application in circularly polarized organic light-emitting diodes (CPOLEDs). The sorption loss to the polarizer can be effectively avoided, and the energy in the CPOLED displays can be saved. Although significant progress has been achieved since the first observation of circularly polarized electroluminescence in chiral conjugated polymers,[7] the high external quantum efficiency (EQE) and small efficiency roll-off remain as challenges. Thermally activated delayed fluorescence (TADF) molecules, which could achieve nearly 100% exciton usage efficiency, are thought as third-generation organic light-emitting materials, and may effectively improve the electroluminescence efficiency. Great efforts have been devoted to TADF materials and high efficiency has been obtained, while the roll-off efficiency is quite severe.[8–12] Aggregation-induced emission (AIE) provides an excellent strategy to solve the problem of roll-off efficiency.[13–17] Thus, the combination of the TADF and AIE properties with the CPL materials are anticipated as promising emitting layers for efficient CPOLEDs.

Recently, a series of chiral AIEgens based on the binaphthalene unit with TADF (R/S-BN-CF, R/S-BN-CCB, R/S-BN-DCB and R/S-BN-AF) were synthesized by Tang' group.[18] High EQEs (up to 9.3% and 3.5%) and electroluminescence dissymmetry factors were achieved for both doped and neat films for these molecules as emitting layers. For all the systems, the binaphthalene unit was used as the chiral unit, while different donor groups were adopted as the TADF units. Due to the limited CPL molecules studied until now, it is of great importance to figure out the relationship between the geometry and the light-emitting properties. It is also quite necessary to reveal the AIE and TADF mechanisms of CPL molecules with high EQE in films. For the AIE phenomenon, several mechanisms such as J aggregation,[19] isomerization,[20] formation of the exciplex,[21] and intramolecular charge transfer[22,23] have been provided.

[a] School of Physics and Optoelectronic Engineering, Shandong University of Technology, 250049 Zibo, China. E-mail: sunyuping@sdut.edu.cn
[b] Shandong Province Key Laboratory of Medical Physics and Image Processing Technology, School of Physics and Electronics, Shandong Normal University, 250014 Jinan, China. E-mail: linll@sdnu.edu.cn, ckwang@sdnu.edu.cn

† Electronic supplementary information (ESI) available: Tables S1, S2 and Fig. S1–S4. See DOI: 10.1039/c9cp00402e

Published on 08 March 2019. Downloaded by Institute of Chemistry, CAS on 3/26/2019 2:21:59 AM.

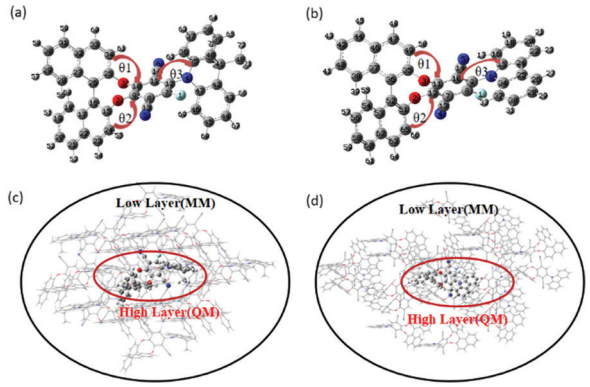

Fig. 1 (a) Chemical structure of S-BN-AF. $\theta1$: (34, 25, 3, 10), $\theta2$: (24, 15, 2, 9), $\theta3$: (11, 12, 4, 35). (b) Chemical structure of R-BN-CF. $\theta1$: (49, 35, 3, 11), $\theta2$: (65, 51, 2, 12), $\theta3$: (10, 9, 6, 15). (c) ONIOM model: surrounding molecules are regarded as the low layer and the centered S-BN-AF is treated as the high layer. (d) ONIOM model: surrounding molecules are regarded as the low layer and the centered R-BN-CF is treated as the high layer.

However, there are still some controversies, and the most popular mechanism is the restricted intramolecular motions submitted by Tang' group.[24] For the TADF mechanism, although the up-conversion from T_1 to S_1 is the first mechanism proposed,[25] it was found to be quite a coarse recent description and assistance from the intermediate local-excited triplet state has been proven to be important.[26–28] In this paper, the R/S-BN-CF and R/S-BN-AF molecules were chosen as models to investigate the geometry–property relationship (as shown in Fig. 1). Theoretical simulations based on combined quantum mechanics and molecular mechanics (QM/MM) and excited-state dynamics can provide detailed information about the light-emitting mechanisms of organic molecules in the solid phase.[29,30] The study of the photophysical properties and excited-state dynamics of R-BN-CF and S-BN-AF in both the solid state and in toluene would reveal the TADF and AIE mechanisms intuitively. Theoretical results will further provide insights on the design of high-efficiency CPL molecules.

Theoretical methods

In our calculations, the geometric and electronic structures for both R/S-BN-CF and R/S-BN-AF in the ground states (S_0) were investigated using the density functional theory (DFT). The time-dependent density functional theory (TD-DFT) was adopted for the optimization of excited states. The polarizable continuum model (PCM) was adopted to include the solvent effect in this paper.[31] Although the TD-DFT method has been widely used for the calculation of excited states, especially for medium and large organic systems, the properties of the excited states were found sensitive to the functionals with different HF proportions (HF%) for different molecules.[32] In this work, the emission wavelengths of R/S-BN-AF and R/S-BN-CF in toluene were calculated using different functionals (as shown in Table 1). It was found that the R-molecules have almost the same emission wavelengths as that of S-molecules calculated with

Table 1 Emission wavelength calculated by different functionals for molecules in toluene. The wavelengths are given in nm (eV in parentheses)

	HF%	R-BN-AF	S-BN-AF	R-BN-CF	S-BN-CF
B3LYP	20	860(1.44)	862(1.44)	655(1.89)	654(1.90)
PBE0	25	772(1.61)	773(1.60)	593(2.09)	592(2.09)
BMK	**42**	**617(2.01)**	**620(2.00)**	**490(2.53)**	**488(2.54)**
M062X	54	535(2.32)	535(2.32)	435(2.85)	434(2.86)
Exp[a]		585	585	495	495

[a] Exp are experimental data.

all the functionals. The emission wavelengths calculated with the BMK functional for R/S-BN-AF and R/S-BN-CF in toluene are 617/620 nm and 490/488 nm, respectively, which is in good agreement with the experimental values (585 nm for R/S-BN-AF and 495 nm for R/S-BN-CF). Therefore, the BMK functional was adopted in our following calculations. The basis set 6-31G(d), which has been found reliable for organic light-emitting molecules, was adopted here.[33] The electronic circular dichroism (ECD) spectra for all the molecules were also calculated using the TD-DFT method at the BMK/6-31G(d) level.

To investigate the properties of both molecules in the solid phase, the QM/MM method with a two-layer ONIOM approach was used.[34,35] The computational models were built based on the X-ray crystal structures of R-BN-CF and S-BN-AF,[36] as shown in Fig. 1(c) and (d). The central molecule was selected as the high layer and was calculated using the QM method, while the surrounding molecules were chosen as the low layer and were simulated using the MM method. Both the DFT and TD-DFT methods were used for the QM calculation, and the BMK/6-31G(d) level was adopted. For the MM section, the universal force field (UFF) was applied, and the electronic embedding was adopted to describe the coupling of the QM/MM interfaces.[37,38] During the QM/MM geometry optimizations for the ground state and excited states, the molecules of the MM part were frozen, and only the QM section was free. All the calculations above were carried out in the Gaussian 16 package.[39]

Furthermore, the normal mode analyses were performed using the DUSHIN program.[40] Based on the stable geometries of all the excited states, the decay rates of all excited states were calculated. For all the systems, the radiative rates for the first excited state (S_1) were calculated using Einstein's spontaneous emission equation:

$$K_r = \frac{f\Delta E_{fi}^2}{1.499} \quad (1)$$

where f is the oscillator strength and ΔE_{fi} is the vertical energy in units of wave numbers (cm^{-1}).

The intersystem crossing (ISC) rate K_{ISC} and reverse intersystem crossing (RISC) rate K_{RISC} between the singlet and triplet states were calculated based on the Marcus rate equation.[41,42]

$$K_{ji} = \frac{V_{ji}^2}{\hbar}\sqrt{\frac{\pi}{K_B T\lambda}}\exp\left[-\frac{(\Delta G_{ji}+\lambda)^2}{4\lambda K_B T}\right] = \frac{V_{ji}^2}{\hbar}\sqrt{\frac{\pi}{K_B T\lambda}}\exp\left[-\frac{\Delta G^{\perp}}{K_B T}\right] \quad (2)$$

Here, V_{ji} is the spin–orbit coupling between the initial state and the final state; the spin–orbit coupling constants between S_1

Published on 08 March 2019. Downloaded by Institute of Chemistry, CAS on 3/26/2019 2:21:59 AM.

and other triplet excited states were calculated using the Dalton2013 package.[43] λ is the reorganization energy which is defined as the energy change during relaxation in two states. ΔG_{ji} represents the energy differences between the two states, and the temperature T was set as 298 K in this work.

Additionally, the non-radiative decay rate for S_1 (K_{nr}) was calculated using the thermally vibrational correlation functional (TVCF) method, which has been realized in the MOMAP (Molecular Materials Property Prediction Package) program.[44–46] For detailed information about the TVCF method, please refer to the ref. 47. Here, we only present some key formulas used.

Based on the first-order perturbation theory and the Fermi-Golden rule, the non-radiative rate K_{nr} can be written as:

$$K_{nr} = \frac{2\pi}{\hbar^2}\sum_{\mu,v} P_{iv}\left|H_{f\mu,iv}\right|^2 \delta\left(E_{iv} - E_{f\mu}\right) \quad (3)$$

The delta function δ is to ensure the conservation of energy. μ and v are vibrational quantum numbers. $H_{f\mu,iv}$ is the interaction between two different Born–Oppenheimer states (f and i), and there are two components in it:

$$\widehat{H}\Psi_{iv} = \widehat{H}^{BO}\Phi_i(r,Q)\Phi_v(Q) + \widehat{H}^{SO}\Phi_i(r,Q)\Phi_v(Q). \quad (4)$$

Here, $\widehat{H}^{BO}$ is the nonadiabatic coupling and $\widehat{H}^{SO}$ is the spin–orbit coupling. The non-radiative decay rate from S_1 to S_0 can be written as:

$$K_{nr} = \frac{2\pi}{\hbar}\sum_{kl} R_{kl} Z_i^{-1} \sum_{v\mu} e^{-\beta E_{iv}} \left\langle \Phi_{f\mu}\middle|\widehat{P}_{fk}\middle|\Phi_{iv}\right\rangle \left\langle \Phi_{iv}\middle|\widehat{P}_{fl}\middle|\Phi_{f\mu}\right\rangle \delta\left(E_{iv} - E_{f\mu}\right) \quad (5)$$

Here, $R_{kl} = \left\langle \Phi_f\middle|\widehat{P}_{fk}\middle|\Phi_i\right\rangle \left\langle \Phi_i\middle|\widehat{P}_{fl}\middle|\Phi_f\right\rangle$ is the nonadiabatic electronic coupling. $\widehat{P}_{fk} = -i\hbar\frac{\partial}{\partial Q_{fk}}$ represents the normal momentum operator of the kth normal mode in the final electronic state. Z_i is the partition function. Based on the Franck–Condon principle, the equation can be written as follows by applying the Fourier transform of the delta function:

$$K_{nr} = \sum_{kl}\frac{1}{\hbar^2}R_{kl}\int_{-\infty}^{\infty} dt\left[e^{i\omega_{if}t} Z_i^{-1}\rho_{IC}(t,T)\right] \quad (6)$$

Here, $\rho_{IC}(t,T)$ is the thermal-vibration correlation function. For TADF systems, the fluorescence efficiency is determined by the prompt fluorescence efficiency (Φ_{PF}) $\Phi_{PF} = \frac{K_r}{K_r + K_{nr} + K_{ISC}}$.

Results and discussion

Molecular geometries

The optimized geometric structures of S-BN-AF and R-BN-CF in toluene are shown in Fig. 1(a) and (b), respectively. The typical geometry parameters of S_0, S_1 and the first triplet excited state (T_1) of S-BN-AF (marked in Fig. 1(a)) are listed in Table 2. The geometric parameters of S-BN-AF in three states (S_0, S_1 and T_1) in toluene are quite different from that in the solid phase. The differences of dihedral angles ($\theta1$ and $\theta2$) for all three states in the two phases range from 2° to 7°, while the variation for $\theta3$ is as large as 39.5°. The differences for $\theta3$ in the two phases may result in significantly different electronic properties and light-emitting properties. When the molecule is excited from S_0 to S_1 or T_1, the geometry also changes in both phases. It is obvious that the differences in the geometry of three states are mainly caused by the changes of the dihedral angles between the donor group and the acceptor group ($\theta3$), both in toluene and in the solid phase. However, the variation in the solid phase is much smaller than that in toluene. It was found that $\theta3$ changes by 10.35° between S_0 and S_1 and by 20.37° between S_1 and T_1 in toluene, while it changes only by 3.11° and 3.56° in the solid phase.

Similarly, three typical dihedral angles (marked in Fig. 1(b)) for R-BN-CF at S_0, S_1 and T_1 are shown in Table 3. It can be found that the variations in dihedral angles $\theta1$ and $\theta2$ have more or less variation when the molecule is excited from S_0 to the excited states. The dihedral angle $\theta3$ accounts for the main configuration differences between the S_0, S_1 and T_1 states. Similar to S-BN-AF, the restricted changes in geometry can be found for R-BN-CF in the solid phase. All these parameters indicate that compared with the situation in the solid phase, the molecules in the solvent are more flexible and easier to change when the molecules are excited. In addition, comparing the geometric parameters of R-BN-CF and S-BN-AF, we can see that the dihedral angles between the donor and the acceptor ($\theta3$) are totally different, which should be induced by different interactions between D and A. The angle for S-BN-AF in the solid phase is 70°, while it is only 45° (−135°) for the R-BN-CF in the solid phase. The difference in $\theta3$ may induce different charge transfer properties for the excited states. The dihedral angles between the chiral group (binaphthalene) and the acceptor group are also different for S-BN-AF and R-BN-CF, which indicates that the change of donor can also influence the interaction of the chiral group and the acceptor group to some extent.

Table 2 Geometric parameters of the S_0, S_1 and T_1 states for S-BN-AF in toluene and the solid phase, respectively. $\theta1$, $\theta2$ and $\theta3$ (marked in Fig. 1(a)) represent the dihedral angles. Δ represents the variation between the two states

	Toluene					Solid				
	S_0	S_1	T_1	$\Delta_{S_1-S_0}$	$\Delta_{S_1-T_1}$	S_0	S_1	T_1	$\Delta_{S_1-S_0}$	$\Delta_{S_1-T_1}$
$\theta1$	85.88	85.97	85.70	0.09	0.27	92.80	91.46	92.08	−1.34	−0.62
$\theta2$	89.38	87.50	88.72	−1.88	−1.22	85.19	85.33	85.63	0.14	−0.30
$\theta3$	98.78	88.43	108.80	−10.35	−20.37	69.76	72.87	69.31	3.11	3.56

Published on 08 March 2019. Downloaded by Institute of Chemistry, CAS on 3/26/2019 2:21:59 AM.

Table 3 Geometric parameters of the S_0, S_1 and T_1 states for R-BN-CF in toluene and the solid phase, respectively. $\theta1$, $\theta2$ and $\theta3$ (marked in Fig. 1(b)) represent the dihedral angles. Δ represents the variation between two states

	Toluene					Solid				
	S_0	S_1	T_1	$\Delta_{S_1-S_0}$	$\Delta_{S_1-T_1}$	S_0	S_1	T_1	$\Delta_{S_1-S_0}$	$\Delta_{S_1-T_1}$
$\theta1$	−87.26	−84.98	−81.40	2.28	−3.58	−88.23	−87.96	−85.86	0.27	−2.10
$\theta2$	−89.54	−87.47	−89.31	2.07	1.84	−82.62	−81.78	−81.35	0.84	−0.43
$\theta3$	−121.69	−102.81	−121.52	18.88	18.71	−135.28	−131.27	−135.92	4.01	4.65

In order to quantitatively characterize the geometric changes during excitation for the molecules, we calculated the root-mean-square deviation (RMSD) between the two states for S-BN-AF and R-BN-CF using Multiwfn.[48] The RMSD values between S_0 and S_1 for S-BN-AF and R-BN-CF are shown in Fig. 2, and the RMSD values between S_1 and other triplet states are collected in Fig. S1 and S2 (ESI†). It can be seen that the geometric changes between S_0 and S_1 for S-BN-AF in toluene (RMSD = 0.312 Å) are more significant than those in the solid phase (RMSD = 0.058 Å). The structural changes of R-BN-CF show a similar trend. The limited geometric variation in rigid environments predicts that the non-radiative energy consumption path is hindered, which may induce enhanced fluorescence efficiency in the solid phase. Moreover, the suppression of geometric change for R-BN-CF in the solid phase is more pronounced than that for S-BN-AF.

For R-BN-AF and S-BN-CF, similar emission wavelengths can be found for their enantiomers S-BN-AF and R-BN-CF (as shown in Table 1). The geometric and electronic structures are also almost the same for the enantiomers. The ECD spectra for the enantiomers are shown in Fig. S3 (ESI†). It was found that the enantiomers have opposite absorption properties. Compared with experimental results, we found that the small peak at 405 nm for R/S-BN-CF and at 436 nm for R/S-BN-AF were missing in the theoretical results. Through detailed analysis, we found that the peak is from a charge-transfer (CT) transition and that functional BMK is known to perform poorly for CT-like transitions owing to an incorrect asymptotic behavior.[49–51] However, the main peaks for the enantiomers are in good agreement with the experimental counterparts.[52] Here, we should note that the peaks at about 405 nm and 436 nm for the two molecules detected experimentally are still quite weak, which also indicates that they are from the absorption of the CT states. Although the oscillator strengths which reflect the intensity of the spectra of the CT states were described poorly by the functional, the excitation energy is quite well obtained. Considering that the excitation energy is quite an important parameter for TADF molecules, it is a tradeoff decision to adopt the BMK functional in all the calculations below. Since similar light-emitting properties for the enantiomers can be found and only the crystal structures of S-BN-AF and R-BN-CF are available, the analysis in this work is mainly based on the study of S-BN-AF and R-BN-CF.

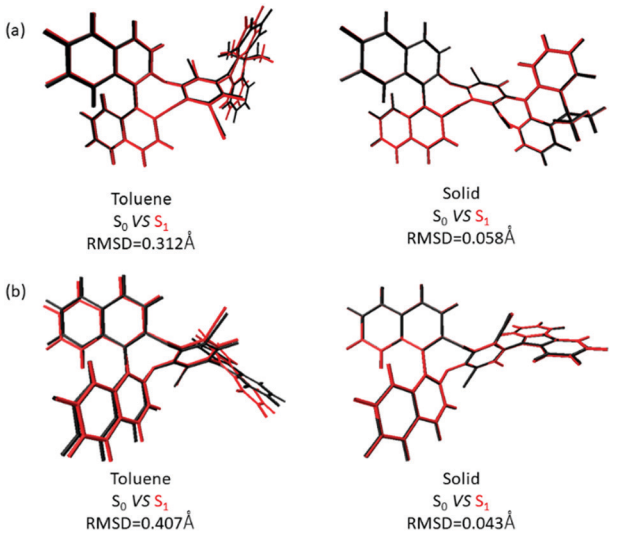

Fig. 2 Visible geometry changes between S_0 (black) and S_1 (red) in toluene and in the solid phase for S-BN-AF (a) and R-BN-CF (b), respectively.

Energy gap and transition property

A small energy gap between S_1 and T_1 is important for the realization of the RISC process in TADF-OLEDs. The adiabatic excitation energies of S-BN-AF and R-BN-CF in toluene and in the solid phase are shown in Fig. 3. It can be seen that the energy landscapes for both molecules are different. For the S-BN-AF molecule, there is only one triplet state (T_1) below S_1, and the S_1–T_1 energy gap is 0.05 eV in both the toluene and solid phases (Fig. 3(a) and (b)). Such a small energy gap can efficiently promote the RISC process from T_1 to S_1 for S-BN-AF. Nevertheless, T_2 is also quite close to S_1 in energy (with T_2 0.05 eV higher in energy than S_1 in toluene and 0.13 eV higher in the solid phase); thus, it also may participate in the ISC and RISC processes. For the R-BN-CF molecule, the energy level structure below S_1 is relatively complex. Four triplet states T_1, T_2, T_3, and T_4 are lower in energy than S_1 with energy gaps of 0.43, 0.34, 0.34 and 0.11 eV in toluene, respectively (Fig. 3(c)). The energy level of T_5 is a little higher than S_1, with a small energy gap of 0.21 eV. According to the Marcus rate equation $K_{RISC} \propto e^{-\Delta E^{ST}/K_BT}$, large energy gaps are not favorable for RISC process. From the energy structure of R-BN-CF in toluene, we can deduce that ISC processes should happen between S_1 and these triplet states (T_1, T_2, T_3, T_4 and T_5), while RISC processes should mainly happen between T_4, T_5 and S_1. The similar energy landscapes can be seen for the R-BN-CF molecule in the solid phase (Fig. 3(d)), for which the four triplet states (T_1, T_2, T_3, T_4) are lower than S_1, and the energy gap is 0.67 eV, 0.49 eV, 0.35 eV and 0.34 eV, respectively. The energy level of T_5 is the closest to S_1, with a small energy gap of 0.07 eV. Based on the energy structure, one can expect that the efficient RISC

This journal is © the Owner Societies 2019

Published on 08 March 2019. Downloaded by Institute of Chemistry, CAS on 3/26/2019 2:21:59 AM.

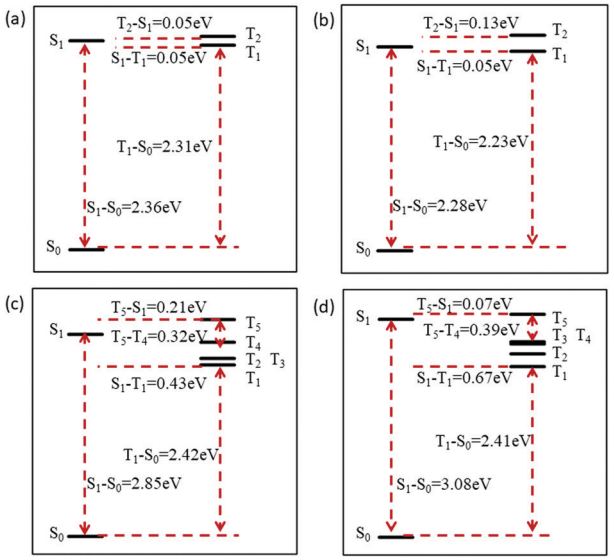

Fig. 3 Adiabatic excitation energies for S-BN-AF in toluene (a) and in the solid phase (b); adiabatic excitation energies for R-BN-CF in toluene (c) and in the solid phase (d) respectively.

process should happen from T_5 to S_1, due to the small T_5–S_1 energy gap. It is noted that the energy difference ΔE_{ST} is important but is not the only index to realize the reverse intersystem crossing. The transition properties and spin–orbit coupling (SOC) between the singlet and triplet excited states also have an important effect on the ISC and RISC processes.

Natural transition orbital (NTO) analysis was performed for S_1 and other triplet states of both molecules in toluene and in the solid phase. The corresponding highest occupied natural transition orbital (HONTO) and the lowest unoccupied natural transition orbital (LUNTO) with transition ratios for S-BN-AF and R-BN-CF are plotted in Fig. 4 and 5, respectively. Combined with the local excitation (LE) ratio of each state (as shown in Tables S1 and S2, ESI†), one can conclude that S_1 of S-BN-AF is a CT state both in toluene and in the solid phase. Although the T_1 states in both toluene and the solid phases are also CT states, the LE components (40.70% and 39.06%) become more significant than that in S_1 (16.31% and 20.56%). The T_2 states in both phases are also CT states, while the variations for the LE component in both phases are more obvious (19.32% and 38.90%). In addition, one can find that the transition for S_1, T_1 and T_2 mainly happens between the donor and the acceptor groups for the S-BN-AF in both phases. The chiral unit has no influence on the transition for all three states of S-BN-AF. The transition properties of the excited states of R-BN-CF in both phases are illustrated in Fig. 5, Fig. S4 and Table S2 (ESI†). One can also note that the transitions for S_1, T_3 and T_4 of R-BN-CF mainly happen between the D and A groups in both phases, while the transitions for T_1 and T_2 have a relationship only with the chiral unit. For T_5, the transition in the solid phase happens between the chiral unit and the acceptor group, while it relies on the D and A groups in toluene. For the R-BN-CF molecule, the T_1, T_2, T_3 and T_4 states are all significant LE states in two phases, and S_1 are typical CT states in both phases.

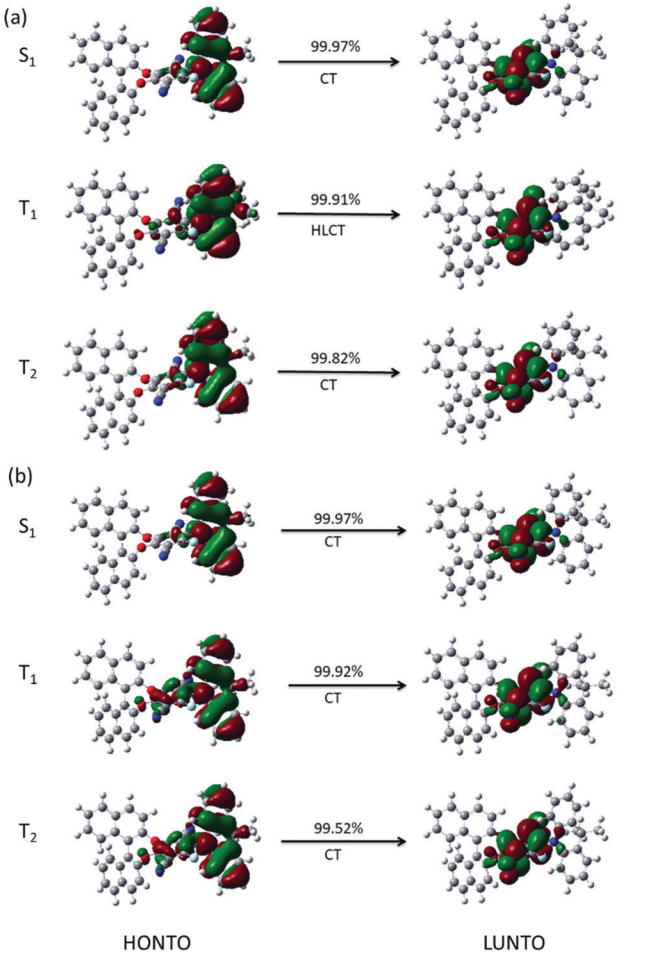

Fig. 4 Transition characteristics for S_1, T_1 and T_2 of S-BN-AF in toluene (a) and in the solid phase (b), respectively. The value above every arrow represents the ratio of depicted NTOs in the corresponding transition.

However, the T_5 changes from a CT state in toluene to an LE state in the solid phase. The corresponding LE ratio of T_5 changes from 32.98% to 74.55% (Table S2, ESI†), which indicates that the T_5 state of R-BN-CF is a stable triplet state in the solid phase. The local excitation feature of the triplet states is conducive to the enhancement of spin–orbit coupling, which is expected for TADF materials to realize the efficient reverse intersystem crossing process.[53,54] From the NTOs of the two molecules, we concluded that the chiral unit would not influence the emission process, since S_1 has no relationship with the transition of S_0. Nevertheless, it may have an effect on the (R)ISC process, because the chiral unit participates in the transition of the triplet states of the R-BN-CF. From our investigation, we also concluded that the variation of donors may also influence the interaction of the chiral unit with the D–A groups and also the transition properties of the triplet excited states.

The spin–orbit coupling between the S_1 and triplet states involved for both molecules studied are listed in Tables 4 and 5, respectively. It was found that all the spin–orbit coupling values in the solid phase were larger than that in toluene, which may favor the (R)ISC process in the solid phase. For S-BN-AF, the

Published on 08 March 2019. Downloaded by Institute of Chemistry, CAS on 3/26/2019 2:21:59 AM.

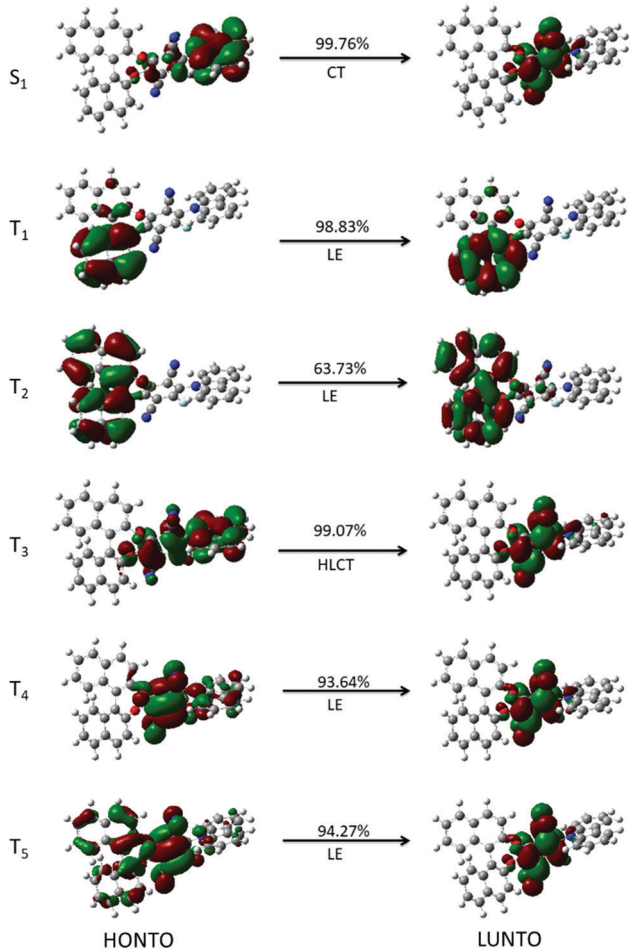

Fig. 5 Transition characteristics for S_1, T_1, T_2, T_3, T_4 and T_5 of R-BN-CF in the solid phase. The value above every arrow represents the ratio of the depicted NTOs in the corresponding transition.

$\langle S_1|H_{SO}|T_1\rangle$ value in the solid phase is about 20 times larger than that in toluene. For R-BN-CF, the spin–orbit coupling between S_1 and T_1, T_3, T_4 and T_5 are all much larger than the $\langle S_1|H_{SO}|T_2\rangle$ value. Through the analysis above, it can be found that the surrounding environment not only influences the geometric structures of both molecules studied, but also the energy landscapes, the transition properties as well as the spin–orbit coupling values of the excited states.

One should note that all the SOC values are smaller than the other organic molecules which are in the range of 1–40 cm^{-1}.[55] This may be a typical characteristic of TADF molecules whose singlet and triplet states have significant CT character.[56] Although the SOC values are small, the small S–T energy gap

Table 4 Calculated spin–orbit coupling constants (in cm^{-1}) between selected singlet and triplet excited states for S-BN-AF in toluene and the solid phase based on the optimized S_1, T_1 and T_2 structures respectively

	Toluene	Solid
$\langle S_1\|H_{SO}\|T_1\rangle$	0.021	0.463
$\langle S_1\|H_{SO}\|T_2\rangle$	0.216	0.262

Table 5 Calculated spin–orbit coupling constants (in cm^{-1}) between the selected singlet and triplet excited states for R-BN-CF in toluene and the solid phase based on the optimized S_1, T_1, T_2, T_3, T_4 and T_5 structures respectively

	Toluene	Solid
$\langle S_1\|H_{SO}\|T_1\rangle$	0.400	0.657
$\langle S_1\|H_{SO}\|T_2\rangle$	0.030	0.083
$\langle S_1\|H_{SO}\|T_3\rangle$	0.294	0.376
$\langle S_1\|H_{SO}\|T_4\rangle$	0.639	0.715
$\langle S_1\|H_{SO}\|T_5\rangle$	0.240	0.577

may induce large ISC or RISC rates.[57] In addition, the radiative rates for TADF molecules are usually smaller than the conventional fluorescent emitters; the ISC and RISC processes would also play a significant role in the excited decay process. Since SOC values are quite dependent on geometric structures,[58] it is possible to obtain larger SOC values when considering contributions from different conformers.[55,59] Thus, the non-adiabatic dynamics should be performed to obtain different samples, which will be further considered in future study.

Huang–Rhys factor and reorganization energy

The non-radiative decay process is closely related to the geometrical distortion and the vibronic coupling between the emissive excited state and the ground state. Thus, to figure out the structure–property relationship during the non-radiative processes, the Huang–Rhys factor (HR) and the reorganization energy (λ) were calculated using the DUSHIN program. HR and λ are defined as $HR_k = \frac{\omega_k D_k^2}{2}$ and $\lambda = \sum_k \hbar\omega_k HR_k$, respectively. Here, ω_k represents the vibration frequency, and D_k is the normal coordinate displacement of mode k. The HR factors and reorganization energy of S-BN-AF and R-BN-CF *versus* the mode frequency are shown in Fig. 6 and 7, respectively. One can

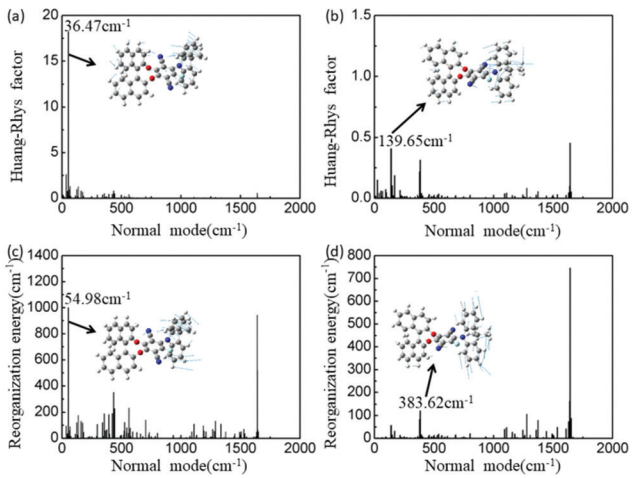

Fig. 6 Calculated HR factors *versus* the normal mode frequencies for S-BN-AF in toluene (a) and in the solid phase (b) as well as the reorganization energies *versus* the normal mode frequencies for S-BN-AF in toluene (c) and in the solid phase (d), respectively. Representative vibration modes are shown as insets.

This journal is © the Owner Societies 2019

Published on 08 March 2019. Downloaded by Institute of Chemistry, CAS on 3/26/2019 2:21:59 AM.

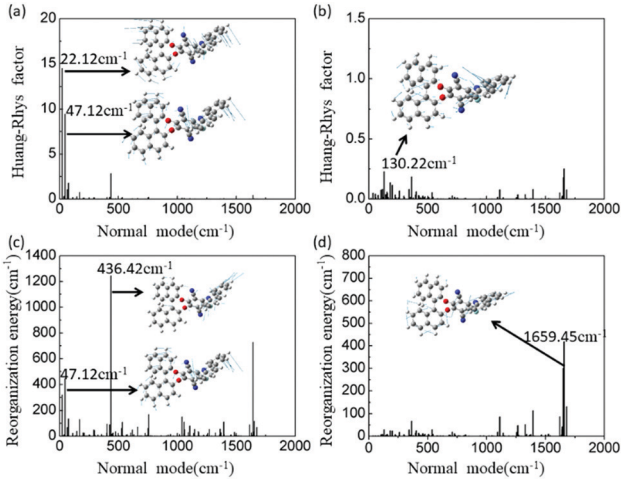

Fig. 7 Calculated HR factors *versus* the normal mode frequencies for R-BN-CF in toluene (a) and in the solid phase (b) as well as the reorganization energies *versus* the normal mode frequencies for R-BN-CF in toluene (c) and in the solid phase (d), respectively. Representative vibration modes are shown as insets.

see that for the S-BN-AF molecule, the remarkable HR factor (18.22) appears in the low-frequency region (36.47 cm^{-1}) in toluene. The HR factor in the solid phase decreased with the largest factor being 0.41 (at the mode with a frequency of 139.65 cm^{-1}), which is about 44 times smaller than that in toluene. The reorganization energies of S-BN-AF are mainly contributed by one low-frequency mode (54.98 cm^{-1}) and one relatively high-frequency mode (1641.21 cm^{-1}) in toluene. In the solid phase, the reorganization energies of S-BN-AF in low-frequency regions sharply decreased, and the vibration in the high-frequency region is also restricted, with the reorganization energy being 117.07 meV (1641.21 cm^{-1}) in toluene and 92.48 meV (1642.92 cm^{-1}) in the solid phase.

For R-BN-CF, the large HR factors all appeared in the low-frequency region in toluene, *e.g.*, 22.12 cm^{-1} and 47.12 cm^{-1}, while the largest HR value in the solid phase was reduced to only about 0.25 (emerging at 130.22 cm^{-1}). Furthermore, the change of reorganization energy from the solvent phase to the solid phase is similar to that of S-BN-AF. The maximal value of reorganization energy decreases from 154.34 meV (436.42 cm^{-1}) in toluene to 51.88 meV (1659.45 cm^{-1}) in the solid phase. One can see that for both molecules studied, the values of HR and λ are significantly reduced in the solid phase because the low-frequency vibrations are effectively restricted. Based on the analysis above, one can deduce that the molecules in the solvent phase are more flexible and easily induce significant relaxation when the molecules are excited. Contrarily, in the solid phase, the relaxation can be effectively hindered by surrounding molecules.

Moreover, compared with S-BN-AF in the solid phase, the contribution of both the low-frequency mode (383.62 cm^{-1}) and the relatively high-frequency mode (1659.45 cm^{-1}) to the reorganization energy for R-BN-CF in the solid phase is much smaller (Fig. 6(d) and 7(d)). The reason can be found from the difference between their chemical structures. The donor of S-BN-AF with two methyl groups is conducive to increasing the spacing between two adjacent units and decreasing the intermolecular interaction, which makes the molecule more flexible and induces stronger vibrations compared with R-BN-CF. In other words, the non-radiative decay of S-BN-AF is much larger than that of R-BN-CF. Therefore, one can speculate that in the aggregate state, R-BN-CF has a higher fluorescence efficiency than S-BN-AF. The corresponding decay rates are analyzed in the following section.

Excited-state dynamics

In order to gain a deep insight into the excited-state dynamics, the radiative (K_r) and non-radiative (K_{nr}) rates from S_1 to S_0, the intersystem crossing rates (K_{ISC}) and the reverse intersystem crossing rates (K_{RISC}) between the selected singlet and triplet excited states of S-BN-AF and R-BN-CF both in toluene and in the solid phase were quantitatively calculated based on the methodology illustrated in Section 2. Furthermore, the prompt fluorescent efficiency (Φ_{PF}) was calculated for comparison with experimental values. The corresponding data are listed in Tables 6 and 7. It can be seen that the radiative decay rate K_r increases from 1.74×10^4 s^{-1} in toluene to 9.85×10^5 s^{-1} in the solid phase for S-BN-AF. For R-BN-CF, K_r in the solid phase (3.45×10^7 s^{-1}) is also larger than that (4.97×10^6 s^{-1}) in toluene. The acceleration of radiation attenuation is due to the increased oscillator strength (f) from toluene to the solid phase. For S-BN-AF, the oscillator strength is increased from 0.0001 in toluene to 0.0058 in the solid phase. For R-BN-CF, the oscillator strength has a similar relationship as that for S-BN-AF. The non-radiative decay rate (K_{nr}) of both molecules in the solid phase is significantly reduced compared with that in toluene. It can be clearly seen that the value of K_{nr} is reduced from 7.50×10^{10} s^{-1} in toluene to 1.88×10^9 s^{-1} in the solid phase for S-BN-AF. For R-BN-CF, K_{nr} was reduced by nearly two orders of magnitude from toluene to the solid phase (1.82×10^{10} s^{-1} → 2.46×10^8 s^{-1}). This confirms our previous deduction that the reduction of HR factor and reorganization energy indicates that the non-radiative decay channel is hindered due to the restricted soft vibrations of the rigid environment in the solid phase.

Table 6 Calculated radiative and non-radiative rates from S_1 to S_0 as well as the ISC and RISC rates between the singlet and triplet excited states (T_1, T_2). The calculated prompt fluorescence efficiency (Φ_{PF}) for S-BN-AF is listed. Corresponding experimental results are also presented with the superscript 'exp'

	Toluene	Solid
$K_r(S_1 \rightarrow S_0)$	1.74×10^4	9.81×10^5
$K_{nr}(S_1 \rightarrow S_0)$	7.50×10^{10}	1.88×10^9
$K_{ISC}(S_1 \rightarrow T_1)$	2.31×10^5	2.12×10^8
$K_{RISC}(T_1 \rightarrow S_1)$	3.29×10^4	3.03×10^7
$K_{ISC}(S_1 \rightarrow T_2)$	10.91	6.63×10^2
$K_{RISC}(T_2 \rightarrow S_1)$	76.48	1.05×10^5
$K_{ISC}^{cal}(S \rightarrow T)$	2.31×10^5	2.12×10^8
$K_{RISC}^{cal}(T \rightarrow S)$	3.29×10^4	3.03×10^7
Φ_{PF}	0.0002‰	0.05%
Φ_{PF}^{exp}	—	4.71%

Published on 08 March 2019. Downloaded by Institute of Chemistry, CAS on 3/26/2019 2:21:59 AM.

Table 7 Calculated radiative and non-radiative rates from S_1 to S_0 as well as the ISC and RISC rates between the singlet and triplet excited states (T_1, T_2, T_3, T_4 and T_5). The calculated prompt fluorescence efficiency (Φ_{PF}) for R-BN-CF is listed. The corresponding experimental result are also presented with the superscript 'exp'

	Toluene	Solid
$K_r(S_1 \rightarrow S_0)$	4.97×10^6	3.45×10^7
$K_{nr}(S_1 \rightarrow S_0)$	1.82×10^{10}	2.46×10^8
$K_{ISC}(S_1 \rightarrow T_1)$	4.07×10^5	6.00×10^7
$K_{ISC}(S_1 \rightarrow T_2)$	8.51×10^4	1.09×10^6
$K_{ISC}(S_1 \rightarrow T_3)$	1.94×10^4	1.43×10^6
$K_{ISC}(S_1 \rightarrow T_4)$	1.20×10^7	2.21×10^7
$K_{ISC}(S_1 \rightarrow T_5)$	1.04	1.91×10^6
$K_{RISC}(T_1 \rightarrow S_1)$	2.18×10^{-2}	2.80×10^{-4}
$K_{RISC}(T_2 \rightarrow S_1)$	1.47×10^{-1}	5.65×10^{-3}
$K_{RISC}(T_3 \rightarrow S_1)$	2.68×10^2	1.72
$K_{RISC}(T_4 \rightarrow S_1)$	2.13	85.51
$K_{RISC}(T_5 \rightarrow S_1)$	3.72×10^3	2.92×10^7
$K_{ISC}^{cal}(S \rightarrow T)$	1.15×10^7	4.73×10^7
$K_{RISC}^{cal}(T \rightarrow S)$	3.47×10^3	2.92×10^7
Φ_{PF}	0.03%	10.52%
Φ_{PF}^{exp}	—	37.5%

Moreover, the K_{ISC} and K_{RISC} between S_1 and other triplet excited states are computed by the Marcus rate equation. It should be noted that although the S_1–T_1 energy gap of S-BN-AF in toluene and in the solid phase is exactly the same (Fig. 3), the K_{ISC} and K_{RISC} in the solid phase (2.12×10^8 s^{-1} and 3.03×10^7 s^{-1}) are much larger than that in toluene (2.31×10^5 s^{-1} and 3.29×10^4 s^{-1}). This is due to the increased spin–orbit coupling effect in the solid phase as shown in Table 4. In addition, we also calculated the ISC and RISC rates between S_1 and T_2. It was found that the rates are all much smaller than those between S_1 and T_1. Thus, the ISC and RISC processes should mainly happen between the S_1 and T_1 states.

For R-BN-CF, the (R)ISC process is much more complicated. From Table 7, we can see that the ISC rates between S_1 and all the triplet states involved in the solid phase are larger than those in toluene. Although the energy gap between S_1 and T_1 is as large as 0.43 eV in toluene and 0.67 eV in the solid phase, the ISC rate is as large as 4.07×10^5 and 6.00×10^7, respectively. However, the S_1–T_1 RISC rates in both phases are quite small, and it is obvious that the RISC process mainly happens between T_5 and S_1. That is to say, the RISC process for R-BN-CF in both phases should be realized by two steps: (1) the up-conversion from T_1 to T_5 with the help of T_2, T_3 and T_4; (2) RISC from T_5 to S_1.

Particularly, in order to compare with experimental values, we calculated the effective K_{ISC} and K_{RISC} rates based on the following formula considering all possible RISC decay channels.

$$K_{ISC}^{cal}(S \rightarrow T) = \frac{K_{S_1-T_1}^2 + K_{S_1-T_2}^2 + K_{S_1-T_3}^2 + K_{S_1-T_4}^2 + K_{S_1-T_5}^2}{K_{S_1-T_1} + K_{S_1-T_2} + K_{S_1-T_3} + K_{S_1-T_4} + K_{S_1-T_5}} \quad (7)$$

$$K_{RISC}^{cal}(T \rightarrow S) = \frac{K_{T_1-S_1}^2 + K_{T_2-S_1}^2 + K_{T_3-S_1}^2 + K_{T_4-S_1}^2 + K_{T_5-S_1}^2}{K_{T_1-S_1} + K_{T_2-S_1} + K_{T_3-S_1} + K_{T_4-S_1} + K_{T_5-S_1}} \quad (8)$$

It can be seen that the K_{RISC}^{cal} rate for the R-BN-CF molecule in the solid phase (2.92×10^7 s^{-1}) is nearly four orders of magnitude larger than that in toluene (3.47×10^3 s^{-1}). Consequently, efficient emission can be expected for R-BN-CF in the solid phase. From Tables 6 and 7, we can see that Φ_{PF} for S-BN-AF and R-BN-CF in the solid phase are 0.05% and 10.52%, respectively, which are much larger than that in toluene. The AIE phenomenon was found for both molecules. In both molecules, not only were the radiative rates significantly enhanced in the solid phase, but the non-radiative rates also decreased to a great extent. Both factors can result in emission enhancement in the solid phase.

Conclusions

In summary, the AIE and TADF mechanism of two light-emitting molecules S-BN-AF and R-BN-CF with CPL properties were investigated. Through analyzing the variation of the dihedral angles and RMSD values of the molecules in both toluene and in the solid phase, we found that the geometrical changes in toluene were much larger than those in the solid phase, especially for the dihedral angles between donors and acceptors. Moreover, the HR and λ of the two molecules calculated in the solid phase are much smaller than those in toluene, which results in smaller non-radiation decay rates in the solid phase. Besides, the radiative decay rates for both molecules are increased in the solid phase. We conclude that AIE is due to the suppressed non-radiative process and enhanced radiative rates in the solid phase. In addition, the adiabatic energy levels, the SOC constants and the transition properties of the excited states were also different to some extent in both phases. Based on the decay rates calculated, we conclude that the TADF mechanism for S-BN-AF and R-BN-CF are different. For S-BN-AF, the up-conversion process mainly happens between T_1 and S_1, while the two-step up-conversion process is involved for R-BN-CF. Although a larger S_1–T_1 energy gap was found for R-BN-CF, a more efficient RISC can be found than that in S-BN-AF. Theoretical calculations indicate that R-BN-CF has a higher luminous efficiency than S-BN-AF, which is in agreement with the experimental results. Our calculations indicate that a tiny modification of the donor groups can significantly influence the geometric structure and energy structure of the molecules as well as their light-emitting mechanisms. In addition, our calculations also indicate that a change of the donor groups may also lead to a blue emission and without the loss of multifunctional properties. Our calculation results provide helpful insights into the design of new-type CPL molecules with AIE and TADF.

Conflicts of interest

There are no conflicts of interest to declare.

Acknowledgements

This work is supported by the National Natural Science Foundation of China (Grant No. 11874242, 21403133 and 11204163). The authors are also thankful for the support from the Taishan Scholar Project of Shandong Province.

Published on 08 March 2019. Downloaded by Institute of Chemistry, CAS on 3/26/2019 2:21:59 AM.

Notes and references

1 R. Carr, N. H. Evans and D. Parker, *Chem. Soc. Rev.*, 2012, **41**, 7673.
2 H. Maeda, Y. Bando, K. Shimomura, I. Yamada, M. Naito, K. Nobusawa, H. Tsumatori and T. Kawai, *J. Am. Chem. Soc.*, 2011, **133**, 9266.
3 J. Kumar, T. Nakashima and T. Kawai, *J. Phys. Chem. Lett.*, 2015, **6**, 3445.
4 C. Wagenknecht, C.-M. Li, A. Reingruber, X.-H. Bao, A. Goebel, Y.-A. Chen, Q. Zhang, K. Chen and J.-W. Pan, *Nat. Photonics*, 2010, **4**, 549.
5 R. Farshchi, M. Ramsteiner, J. Herfort, A. Tahraoui and H. T. Grahn, *Appl. Phys. Lett.*, 2011, **98**, 162508.
6 D.-Y. Kim, *J. Korean Phys. Soc.*, 2006, **49**, S505.
7 E. Peeters, M. P. Christiaans, R. A. Janssen, H. F. Schoo, H. P. Dekkers and E. W. Meijer, *J. Am. Chem. Soc.*, 1997, **119**, 9909.
8 J. X. Chen, W. Liu, C. J. Zheng, K. Wang, K. Liang, Y. Z. Shi, X. M. Ou and X. H. Zhang, *ACS Appl. Mater. Interfaces*, 2017, **9**, 8848.
9 T. Liu, L. Zhu, C. Zhong, G. Xie, S. Gong, J. Fang, D. Ma and C. Yang, *Adv. Funct. Mater.*, 2017, **27**, 1606384.
10 X. Tian, H. Sun, Q. Zhang and C. Adachi, *Chin. Chem. Lett.*, 2016, **27**, 1445.
11 T. Sato, M. Uejima, K. Tanaka, H. Kaji and C. Adachi, *J. Mater. Chem. C*, 2015, **3**, 870.
12 J.-z. Fan, S. Qiu, L.-l. Lin and C.-k. Wang, *Chin. Chem. Lett.*, 2016, **29**, 291.
13 J. Fan, Y. Zhang, Y. Zhou, L. Lin and C.-K. Wang, *J. Phys. Chem. C*, 2018, **122**, 2358.
14 Y. Wang, G. Zhang, M. Gao, Y. Cai, C. Zhan, Z. Zhao, D. Zhang and B. Z. Tang, *Faraday Discuss.*, 2017, **196**, 9.
15 X. Zheng, Q. Peng, L. Zhu, Y. Xie, X. Huang and Z. Shuai, *Nanoscale*, 2016, **8**, 15173.
16 H. Tsujimoto, D. G. Ha, G. Markopoulos, H. S. Chae, M. A. Baldo and T. M. Swager, *J. Am. Chem. Soc.*, 2017, **139**, 4894.
17 L. Q. Yan, Z. N. Kong, Y. Xia and Z. J. Qi, *New J. Chem.*, 2016, **40**, 7061.
18 F. Song, Z. Xu, Q. Zhang, Z. Zhao, H. Zhang, W. Zhao, Z. Qiu, C. Qi, H. Zhang, H. H. Y. Sung, I. D. Williams, J. W. Y. Lam, Z. Zhao, A. Qin, D. Ma and B. Z. Tang, *Adv. Funct. Mater.*, 2018, **28**, 1800051.
19 B.-K. An, S.-K. Kwon, S.-D. Jung and S. Y. Park, *J. Am. Chem. Soc.*, 2002, **124**, 14410.
20 Z. Xie, B. Yang, F. Li, G. Cheng, L. Liu, G. Yang, H. Xu, L. Ye, M. Hanif, S. Liu, D. Ma and Y. Ma, *J. Am. Chem. Soc.*, 2005, **41**, 14152.
21 Y. Liu, X. Tao, F. Wang, J. Shi, J. Sun, W. Yu, Y. Ren, D. Zou and M. Jiang, *J. Phys. Chem. C*, 2007, **17**, 6544.
22 R. Hu, E. Lager, A. Aguilar-Aguilar, J. Liu, J. W. Y. Lam, H. H. Y. Sung, I. D. Williams, Y. Zhong, K. S. Wong, E. Peña-Cabrera and B. Z. Tang, *J. Phys. Chem. C*, 2009, **36**, 15845.
23 B.-R. Gao, H.-Y. Wang, Y.-W. Hao, L.-M. Fu, H.-H. Fang, Y. Jiang, L. Wang, Q.-D. Chen, H. Xia, L.-Y. Pan, Y.-G. Ma and H.-B. Sun, *J. Phys. Chem. B*, 2010, **1**, 128.
24 J. Mei, Y. Hong, J. W. Lam, A. Qin, Y. Tang and B. Z. Tang, *Adv. Mater.*, 2014, **26**, 5429.
25 H. Uoyama, K. Goushi, K. Shizu, H. Nomura and C. Adachi, *Nature*, 2012, **492**, 234.
26 M. K. Etherington, J. Gibson, H. F. Higginbotham, T. J. Penfold and A. P. Monkman, *Nat. Commun.*, 2016, **7**, 13680.
27 J. Gibson, A. P. Monkman and T. J. Penfold, *ChemPhysChem*, 2016, **17**, 2956.
28 X.-K. Chen, S.-F. Zhang, J.-X. Fan and A.-M. Ren, *J. Phys. Chem. C*, 2015, **119**, 9728.
29 B. Wang, X. Wang, W. Wang and F. Liu, *J. Phys. Chem. C*, 2016, **120**, 21850.
30 J. Tomasi, B. Menucci and R. Cammi, *Chem. Rev.*, 2005, **105**, 2999.
31 T. Zhang, W. Shi, D. Wang, S. Zhuo, Q. Peng and Z. Shuai, *J. Mater. Chem. C*, 2019, **7**, 1388.
32 S. Huang, Q. Zhang, Y. Shiota, T. Nakagawa, K. Kuwabara, K. Yoshizawa and C. Adachi, *J. Chem. Theory Comput.*, 2013, **9**, 3872.
33 L. Lin, J. Fan, L. Cai and C.-K. Wang, *Mol. Phys.*, 2017, **116**, 19.
34 L. W. Chung, W. M. Sameera, R. Ramozzi, A. J. Page, M. Hatanaka, G. P. Petrova, T. V. Harris, X. Li, Z. Ke, F. Liu, H. B. Li, L. Ding and K. Morokuma, *Chem. Rev.*, 2015, **115**, 5678.
35 K. Zhang, L. Cai, J. Fan, Y. Zhang, L. Lin and C. K. Wang, *Spectrochim. Acta, Part A*, 2019, **209**, 248.
36 J. Fan, L. Cai, L. Lin and C. K. Wang, *Phys. Chem. Chem. Phys.*, 2017, **19**, 29872.
37 J. Fan, L. Cai, L. Lin and C. K. Wang, *J. Phys. Chem. A*, 2016, **120**, 9422.
38 J. Fan, L. Lin and C.-K. Wang, *Phys. Chem. Chem. Phys.*, 2017, **19**, 30147.
39 M. J. Frisch, G. W. Trucks, H. B. Schlegel, G. E. Scuseria, M. A. Robb, J. R. Cheeseman, G. Scalmani, V. Barone, G. A. Petersson, H. Nakatsuji, X. Li, M. Caricato, A. V. Marenich, J. Bloino, B. G. Janesko, R. Gomperts, B. Mennucci, H. P. Hratchian, J. V. Ortiz, A. F. Izmaylov, J. L. Sonnenberg, F. D. Williams, F. Lipparini, F. Egidi, J. Goings, B. Peng, A. Petrone, T. Henderson, D. Ranasinghe, V. G. Zakrzewski, J. Gao, N. Rega, G. Zheng, W. Liang, M. Hada, M. Ehara, K. Toyota, R. Fukuda, J. Hasegawa, M. Ishida, T. Nakajima, Y. Honda, O. Kitao, H. Nakai, T. Vreven, K. Throssell, J. A. Montgomery Jr., J. E. Peralta, F. Ogliaro, M. J. Bearpark, J. J. Heyd, E. N. Brothers, K. N. Kudin, V. N. Staroverov, T. A. Keith, R. Kobayashi, J. Normand, K. Raghavachari, A. P. Rendell, J. C. Burant, S. S. Iyengar, J. Tomasi, M. Cossi, J. M. Millam, M. Klene, C. Adamo, R. Cammi, J. W. Ochterski, R. L. Martin, K. Morokuma, O. Farkas, J. B. Foresman and D. J. Fox, *Gaussian 16 Rev. A.03*, Wallingford, CT, 2016.
40 J. R. Reimers, *J. Chem. Phys.*, 2001, 9103.
41 L. Lin, Z. Wang, J. Fan and C. Wang, *Org. Electron.*, 2017, **41**, 17.
42 O. Vahtras, H. Ågren, P. Jo/rgensen, H. J. r. A. Jensen, T. Helgaker and J. Olsen, *J. Chem. Phys.*, 1992, **97**, 9178.
43 Dalton, A Molecular Electronic Structure Program, http://daltonprogram.org.

Published on 08 March 2019. Downloaded by Institute of Chemistry, CAS on 3/26/2019 2:21:59 AM.

44 J. R. Reimers, *J. Chem. Phys.*, 2001, **115**, 9103.
45 Q. Peng, Q. Shi, Y. Niu, Y. Yi, S. Sun, W. Li and Z. Shuai, *J. Mater. Chem. C*, 2016, **4**, 6829.
46 H. Ma, W. Shi, J. Ren, W. Li, Q. Peng and Z. Shuai, *J. Phys. Chem. Lett.*, 2016, **7**, 2893.
47 Q. Peng, D. Fan, R. Duan, Y. Yi, Y. Niu, D. Wang and Z. Shuai, *J. Phys. Chem. C*, 2017, **121**, 13448.
48 F. C. T. Lu, *J. Comput. Chem.*, 2012, 580.
49 A. Dreuw and M. Head-Gordon, *J. Am. Chem. Soc.*, 2004, **126**, 4007.
50 A. Dreuw and M. Head-Gordon, *Chem. Rev.*, 2005, **105**, 4009.
51 C. Adamo and D. Jacquemin, *Chem. Soc. Rev.*, 2013, **42**, 845.
52 J.-Z. Fan, L.-L. Lin and C.-K. Wang, *Chem. Phys. Lett.*, 2016, **652**, 16.
53 J. Gibson and T. J. Penfold, *Phys. Chem. Chem. Phys.*, 2017, **19**, 8428.
54 P. K. Samanta, D. Kim, V. Coropceanu and J. L. Bredas, *J. Am. Chem. Soc.*, 2017, **139**, 4042.
55 M. Marazzi, S. Mai, D. Roca-Sanjuan, M. G. Delcey, R. Lindh, L. Gonzalez and A. Monari, *J. Phys. Chem. Lett.*, 2016, **7**, 622.
56 L. Lin, L. Cai, J. Fan and C.-K. Wang, *J. Phys. Chem. C*, 2018, **122**, 19953.
57 J. Fan, L. Lin and C.-K. Wang, *J. Mater. Chem. C*, 2017, **5**, 8390.
58 D. Beljonne, Z. Shuai, G. Pourtois and J. L. Bredas, *J. Phys. Chem. A*, 2001, **105**, 3899.
59 O. Sengul, M. Marazzi, A. Monari and S. Catak, *J. Phys. Chem. C*, 2018, **122**, 16315.

 This journal is © the Owner Societies 2019